

Pair correlation of giant halo nuclei in continuum Skyrme-Hartree-Fock-Bogoliubov theory

Y. Zhang,^{1,2,*} M. Matsuo,^{2,3} and J. Meng^{1,4,5}

¹*State Key Laboratory of Nuclear Physics and Technology,
School of Physics, Peking University, Beijing 100871, China*

²*Graduate School of Science and Technology,
Niigata University, Niigata 950-2181, Japan*

³*Department of Physics, Faculty of Science,
Niigata University, Niigata 950-2181, Japan*

⁴*School of Physics and Nuclear Energy Engineering,
Beihang University, Beijing 100191, China*

⁵*Department of Physics, University of Stellenbosch, Stellenbosch, South Africa*

Abstract

The giant halos predicted in neutron-rich Zr isotopes with $A = 124 - 138$ are investigated by using the self-consistent continuum Skyrme Hartree-Fock-Bogoliubov approach, in which the asymptotic behavior of continuum quasiparticle states is properly treated by the Green's function method. We study in detail the neutron pair correlation involved in the giant halo by analyzing the asymptotic exponential tail of the neutron pair condensate (pair density) in addition to that of the neutron particle density. The neutron quasiparticle spectra associated with these giant halo nuclei are examined. It is found that the asymptotic exponential tail of the neutron pair condensate is dominated by non-resonant continuum quasiparticle states corresponding to the scattering states with low asymptotic kinetic energy. This is in contrast to the asymptotic tail of the neutron density, whose main contributions arise from the resonant quasiparticle states corresponding to the weakly-bound single-particle orbits and resonance orbits in the Hartree-Fock potential.

PACS numbers: 21.10.Gv 21.10.Pc, 21.60.Jz, 27.60.+j

*e-mail: yzhangjcn@pku.edu.cn

I. INTRODUCTION

The pairing properties in weakly bound nuclei have drawn a lot of attention since the first halo phenomenon was discovered in ^{11}Li [1]. However, the halos observed so far have only one or two nucleons in the light exotic nuclei. In order to study the influence of correlations and many-body effects, it would be very interesting to investigate the nuclei with a larger number of neutrons distributed in the halo. For this purpose, probable halo phenomena have been searched for in heavier neutron-rich nuclei [2].

The Hartree-Fock-Bogoliubov (HFB) theory [2–9] is a powerful tool to describe the heavier neutron-rich nuclei. It can provide a unified and self-consistent description of both the mean field and pairing correlations in terms of the Bogoliubov quasiparticles. Thus, the pairing properties in nuclei near the drip-line have been studied extensively within the relativistic Hartree-(Fock)-Bogoliubov scheme [2, 7–18] as well as the non-relativistic HFB scheme [4, 5, 13, 19–29].

The giant neutron halo with more than two neutrons is predicted first by the relativistic continuum Hartree-Bogoliubov (RCHB) theory [10] for neutron-rich Zr [2, 11] and Ca [11–13] isotopes. It is found that the radius of the neutron density distribution shows an abnormal increase for $A > 60$ in Ca and $A > 122$ in Zr isotopes. It has been shown later that the non-relativistic Skyrme HFB model can also describe the giant neutron halo in these elements as far as appropriate parameter sets are chosen [13, 26]. Recently, the giant halo is also predicted in Ce isotopes by the relativistic Hartree-Fock-Bogoliubov (RHFB) theory [30].

In the preceding works, focuses are often put on the extended tail of the neutron densities which leads to the abnormal increase of the root-mean-square (r.m.s.) radius of a halo nucleus. It has been discussed that the pair correlation can produce the halo tail of the particle density via the continuum coupling [2, 4, 7, 12] and also suppress the asymptotic particle density distribution due to the additional binding [19, 25, 26, 29]. On the other hand, properties of the pair density or the pairing tensor, which represents the condensate of the nucleon pair, especially those in the low-density halo region, have not been studied in detail. In this paper, we would like to investigate how the neutron pair density behaves in the asymptotic halo region, and also what mechanisms govern its asymptotic behaviors.

Useful information in analyzing the above properties is the spectrum of the neutron quasiparticle states. Because of the shallow Fermi energy, most of the quasiparticle states

are embedded in the continuum energy region by a coupling to the scattering states via the pair potential [3, 4, 6, 31]. In the standard HFB calculations [2–20, 25, 29], a finite box or a harmonic oscillator/Woods-Saxon basis is adopted. In this case the continuum quasiparticle states are all discretized (hereafter referred to as the discretized HFB approach), making it difficult to describe the asymptotic behavior and to quantify the spectra in terms of, e.g., the resonance energy and the width. There exist techniques to overcome this problem, for instance, using a very large box [19, 25], or adopting the analytical continuation in the coupling constant method [32, 33], or the stabilization method [34, 35], or Gamow HFB approach [36]. In the present work, we adopt a new formulation of the Skyrme HFB model in which the Green’s function method [31] is adopted to describe precisely the asymptotic behavior of scattering waves for the unbound quasiparticle states in the continuum (hereafter referred to as the continuum HFB approach) [27, 28].

In this paper we will apply this self-consistent continuum Skyrme HFB approach with Green’s function method [28] to study the pairing properties in the giant halo Zr nuclei. In section II, we will briefly describe the formulation of the continuum Skyrme HFB theory with the Green’s function method and the numerical details. We will also examine the significance of the continuum in the description of the pairing properties by comparing with the results obtained by the discretized HFB approach. After presenting the results and discussions in Sections III–V we draw conclusions in Section VI.

II. FORMALISM

The fundamental building block of the the Hartree-Fock-Bogoliubov (HFB) theory is the quasiparticle states. The energy E and the wave function $\phi_i(\mathbf{r}\sigma)$ of a quasiparticle state obeys the HFB equation

$$\int d\mathbf{r}' \sum_{\sigma'} \begin{pmatrix} h(\mathbf{r}\sigma, \mathbf{r}'\sigma') - \lambda\delta(\mathbf{r} - \mathbf{r}')\delta_{\sigma\sigma'} & \tilde{h}(\mathbf{r}\sigma, \mathbf{r}'\sigma') \\ \tilde{h}^*(\mathbf{r}\tilde{\sigma}, \mathbf{r}'\tilde{\sigma}') & -h^*(\mathbf{r}\tilde{\sigma}, \mathbf{r}'\tilde{\sigma}') + \lambda\delta(\mathbf{r} - \mathbf{r}')\delta_{\sigma\sigma'} \end{pmatrix} \phi_i(\mathbf{r}'\sigma') = E_i \phi_i(\mathbf{r}\sigma), \quad (1)$$

where λ is the Fermi energy. The Hartree-Fock (HF) Hamiltonian h and the pair Hamiltonian \tilde{h} can be obtained by the variation of the total energy functional with respect to the particle density matrix $\rho(\mathbf{r}\sigma, \mathbf{r}'\sigma') = \langle \psi^\dagger(\mathbf{r}'\sigma') \psi(\mathbf{r}\sigma) \rangle$ and pair density matrix $\tilde{\rho}(\mathbf{r}\sigma, \mathbf{r}'\sigma') = \langle \psi(\mathbf{r}'\tilde{\sigma}') \psi(\mathbf{r}\sigma) \rangle$, respectively.

For the spherical system, the quasiparticle wave function can be written as

$$\phi_i(\mathbf{r}\sigma) = \frac{1}{r}\phi_{lj}(r)Y_{ljm}(\hat{\mathbf{r}}\sigma), \quad \text{where} \quad \phi_{lj}(r) = \begin{pmatrix} \varphi_{1,lj}(r) \\ \varphi_{2,lj}(r) \end{pmatrix}. \quad (2)$$

The local particle density $\rho(\mathbf{r}) = \sum_{\sigma} \rho(\mathbf{r}\sigma, \mathbf{r}\sigma)$ and the pair density $\tilde{\rho}(\mathbf{r}) = \sum_{\sigma} \tilde{\rho}(\mathbf{r}\sigma, \mathbf{r}\sigma)$ consist of the products of the quasiparticle wave functions summed up over all the states. Using the Green's function technique, the local densities are expressed [27, 28, 31] as

$$\rho(r) = \frac{1}{4\pi r^2} \sum_{lj} (2j+1) \frac{1}{2\pi i} \oint_{C_E} dE \mathcal{G}_{0,lj}^{11}(r, r, E), \quad (3a)$$

$$\tilde{\rho}(r) = \frac{1}{4\pi r^2} \sum_{lj} (2j+1) \frac{1}{2\pi i} \oint_{C_E} dE \mathcal{G}_{0,lj}^{12}(r, r, E), \quad (3b)$$

where $\mathcal{G}_{0,lj}^{11}(r, r, E)$ and $\mathcal{G}_{0,lj}^{12}(r, r, E)$ are the radial HFB Green's functions. The Green's functions are constructed from the independent solutions of the radial HFB equation (1) with proper boundary conditions for the wave function $\phi_{lj}(r, E)$ of the quasiparticle states with energy E . Similarly, one can express other local densities needed in the Skyrme functional, such as kinetic energy density, spin-orbit densities, etc., in terms of the Green's functions. The integrals in Eqs. (3) are contour integrals in the complex E plane, and the integration path C_E is chosen to be a rectangle with a height $\gamma = 0.1$ MeV and a length $E_{\text{cut}} = 70$ MeV, which symmetrically encloses the real negative quasiparticle energy axis as in Ref. [28]. The energy step of the contour integration is $\Delta E = 0.01$ MeV. We choose the box size $R_{\text{box}} = 20$ fm, and the mesh size $\Delta r = 0.2$ fm for the Runge-Kutta algorithm to obtain the independent solution of the radial HFB equation. The quasiparticle wave functions are connected at $r = R_{\text{box}}$ to the asymptotic wave $\phi_{lj}^{(\text{out})}(r, E)/r = \left(Ah_l^{(+)}(k_+r), Bh_l^{(+)}(k_-r) \right)^T$ where $h_l^{(+)}(z)$ is the spherical Hankel function [37] and $k_{\pm}(E) = \sqrt{2m(\lambda \pm E)/\hbar^2}$. Other details can be found in Ref. [28].

We employ the Skyrme functional SkI4 [38], following Ref. [26], with which the giant halo phenomenon in the Zr isotopes can be reproduced as predicted in the RCHB theory [2]. For the pairing interaction, we adopt the density-dependent delta interaction (DDDI). The difference between the zero range and finite range pairing interaction for exotic neutron rich nucleus has been discussed in Ref. [39]. The pair field here is taken as

$$\Delta(\mathbf{r}) = \frac{1}{2}V_0 \left[1 - \eta \left(\frac{\rho_q(\mathbf{r})}{\rho_0} \right)^{\alpha} \right] \tilde{\rho}(\mathbf{r}), \quad q = n \text{ or } p. \quad (4)$$

The parameters in Eq. (4) are adopted as $V_0 = -458.4 \text{ MeV fm}^{-3}$, $\eta = 0.71$, $\alpha = 0.59$, and $\rho_0 = 0.08 \text{ fm}^{-3}$ [40–43], which reproduce the experimental neutron pairing gap along the Sn isotopic chain. In particular, the parameter V_0 is chosen in such a way that the DDDI reproduces the 1S scattering length $a = -18.5 \text{ fm}$ of the bare nuclear force in the low density limit $\rho(r) \rightarrow 0$, i.e., in the free space outside the nucleus. The quasiparticle states are truncated at the maximal angular momentum $j_{\text{max}} = 15/2$ and at the maximal quasiparticle energy $E_{\text{cut}} = 70 \text{ MeV}$ [26].

For the sake of comparison, we also perform a box-discretized HFB calculation. In this case the HFB equation (1) is solved with the box boundary condition, i.e. by assuming that the wave functions of the quasiparticles vanish at the box boundary $r = R_{\text{box}}$. The discretized quasiparticle wave functions thus obtained, $\phi_{nlj}(\mathbf{r}\sigma)$, are summed up to construct the densities as

$$\rho(r) = \frac{1}{4\pi r^2} \sum_{lj} (2j+1) \sum_n \varphi_{2,nlj}^2(r), \quad (5a)$$

$$\tilde{\rho}(r) = \frac{1}{4\pi r^2} \sum_{lj} (2j+1) \sum_n \varphi_{1,nlj}(r) \varphi_{2,nlj}(r). \quad (5b)$$

III. PAIR CORRELATION IN GIANT NEUTRON HALO NUCLEUS

The filled circles in Fig. 1(a) are the two-neutron separation energy $S_{2n}(N, Z) = E(N, Z) - E(N-2, Z)$, where $E(N, Z)$ is the total binding energy of the isotope with N neutrons and Z protons obtained in the continuum HFB calculation. It suddenly drops from $S_{2n} = 4.81 \text{ MeV}$ at ^{122}Zr to $S_{2n} = 0.64 \text{ MeV}$ at ^{124}Zr as the neutron number exceeds the magic number $N = 82$. Then it gradually decreases to an extremely small value 0.04 MeV at ^{138}Zr , and finally becomes negative in ^{140}Zr . Thus ^{138}Zr is the neutron drip-line nucleus in the present model, which is consistent with the previous investigation [26]. The small two-neutron separation energy is one of the conditions for the emergence of the halo structure. Figure 1 (b) shows the neutron Fermi energy λ as well as the Hartree-Fock (HF) single-particle energies ε , which are the eigen energies of HF Hamiltonian h (obtained after the final convergence of the continuum HFB calculation). One can see that, as the neutron number increases, the Fermi energy is raised up, to a position quite close to the continuum threshold, while all the HF single-particle orbits fall down. Explicitly, the $3p_{1/2}$, $3p_{3/2}$ and

$2f_{7/2}$ states evolve from unbound resonances ($A \leq 122$) to weakly bound orbits ($A \gtrsim 126$), and the $2f_{5/2}$ orbit remains as a resonance in the continuum. The values of these HF single-particle energies in $^{124}\text{Zr} \sim ^{138}\text{Zr}$ can be found in Table I. The HF Hamiltonian has another resonance $1h_{9/2}$ which lies slightly higher than the plotted energy region in Fig. 1 (b).

Figure 2 (a) shows the neutron density $\rho(r)$ calculated for the Zr isotopes with $A = 122 - 138$ using the continuum HFB calculation (solid lines). It is seen that the neutron density for $A = 124 - 138$ exhibits a long tail extending far outside the nuclear surface compared with $A = 122$. Figure 2 (b) shows the r.m.s. radius $r_{\text{r.m.s.}} \equiv [\int 4\pi r^4 \rho(r) dr / \int 4\pi r^2 \rho(r) dr]^{1/2}$ calculated for the corresponding neutron density (filled circles). Compared with the isotopic trend in $A \leq 122$, which gives an extrapolation as $r_{\text{r.m.s.}} \approx 0.87N^{1/3}$ fm, the neutron r.m.s. radius in ^{124}Zr and the heavier isotopes displays a steep increase with N . These results are consistent with the previous investigations in Refs. [2] and [26], where the giant halo structure, i.e. the long tail which can accommodate more than two neutrons, is predicted in the isotopes with $A \geq 124$.

Figure 2 (c) shows the neutron pair density $\tilde{\rho}(r)$. We clearly see that the pair density has an even more significant tail, which is characterized by i) $\tilde{\rho}(r) > \rho(r)$ for $r \gtrsim 10$ fm, and ii) that $\tilde{\rho}(r)$ has a more gentle slope than $\rho(r)$. These features are reflected in the r.m.s. radius weighted with the neutron pair density, $\tilde{r}_{\text{r.m.s.}} \equiv [\int 4\pi r^4 \tilde{\rho}(r) dr / \int 4\pi r^2 \tilde{\rho}(r) dr]^{1/2}$, which is plotted in Fig. 2 (d). We shall call $\tilde{r}_{\text{r.m.s.}}$ the pair r.m.s. radius hereafter. It is significantly larger than $r_{\text{r.m.s.}}$ of the neutron density. Also, the neutron pair r.m.s. radius $\tilde{r}_{\text{r.m.s.}}$ exhibits a sudden jump at ^{124}Zr , and remains almost the same until the drip-line. Here, $\tilde{r}_{\text{r.m.s.}}$ of ^{122}Zr is omitted in the plot due to the absence of pairing.

It is argued in Refs. [2] and [26] that the neutron orbits $3p_{1/2}, 3p_{3/2}, 2f_{5/2}$ and $2f_{7/2}$ around the Fermi energy play a decisive role in forming the giant halo structure in the neutron density. Similarly to Refs. [2] and [26], we decompose the neutron density with respect to different partial waves lj , and calculate separately the r.m.s. radius

$$r_{\text{r.m.s.},lj} = \left(\frac{\int 4\pi r^4 \rho_{lj}(r) dr}{\int 4\pi r^2 \rho_{lj}(r) dr} \right)^{1/2} \quad (6)$$

weighted by the corresponding lj -decomposed neutron density

$$\rho_{lj}(r) = \frac{(2j+1)}{4\pi r^2} \frac{1}{2\pi i} \oint_{C_E} dE \mathcal{G}_{0,lj}^{(11)}(r, r, E), \quad (7)$$

which sums the contributions from the quasiparticles with the quantum number lj within $E = 0 \sim E_{\text{cut}}$. The r.m.s. radii for $lj = s_{1/2}, p_{1/2}, p_{3/2}, d_{3/2}, d_{5/2}, f_{5/2}$ and $f_{7/2}$ partial

waves are plotted (filled symbols) in Fig. 3. We can see clearly that the increase of the total r.m.s. radius is mainly contributed by the p and f states, in agreement with Refs. [2, 26].

The pair density displays an apparently different behavior from that of the neutron density as seen in Fig. 4, in which we plot the neutron pair r.m.s. radius

$$\tilde{r}_{\text{r.m.s.},lj} = \left(\frac{\int 4\pi r^4 \tilde{\rho}_{lj}(r) dr}{\int 4\pi r^2 \tilde{\rho}_{lj}(r) dr} \right)^{1/2}, \quad (8)$$

weighted by the lj -decomposed neutron pair density

$$\tilde{\rho}_{lj}(r) = \frac{(2j+1)}{4\pi r^2} \frac{1}{2\pi i} \oint_{C_E} dE \mathcal{G}_{0,lj}^{(12)}(r, r, E). \quad (9)$$

A notable feature is that the jump at $N = 124$ is seen not only for the partial waves $p_{1/2}, p_{3/2}, f_{5/2}$ and $f_{7/2}$, which have HF single-particle orbits or resonances near the Fermi energy, but also for the partial waves $s_{1/2}, d_{3/2}$ and $d_{5/2}$. This indicates that the s - and d -waves also play important roles in the large tail of the pair density.

To clarify the difference, we present in Fig. 5 the composition of the neutron density $\rho(r)$ and pair density $\tilde{\rho}(r)$ with respect to the partial waves lj , i.e., $\rho_{lj}(r)/\rho(r)$ and $\tilde{\rho}_{lj}(r)/\tilde{\rho}(r)$ for ^{126}Zr and ^{138}Zr . As shown in the previous works [2] and [26], the most dominant compositions of the neutron density $\rho(r)$ in the halo region $r \gtrsim 10$ fm are the p -waves, and the next are the f -waves, while the s - and d -waves as well as others partial waves have very little contributions, and almost vanish at large distances $r \gtrsim 15$ fm.

For the pair density $\tilde{\rho}(r)$, however, we can see from Fig.5 (c) and (d) that the partial wave composition is very different from that of the neutron density $\rho(r)$. The dominance of the waves $p_{1/2}, p_{3/2}, f_{5/2}$ and $f_{7/2}$ is commonly seen also for the pair density, but to a less extent. The waves $s_{1/2}, d_{3/2}$ and $d_{5/2}$, on the other hand, have small but non-negligible contributions in the halo region $r \gtrsim 10$ fm. This feature becomes even stronger in ^{138}Zr than in ^{126}Zr . Since there is no bound HF single-particle orbits nor resonance orbits in the s - and d -waves near the Fermi energy, it is non-resonant continuum orbits that contribute to the pair density.

Before closing this section, we would like to compare the present results obtained in the continuum HFB calculation with those obtained in the box-discretized HFB calculation. In the latter case, the quasiparticle states are discretized even in the continuum energy region $E > |\lambda|$, and the densities are obtained as Eq. (5).

The two-neutron separation energy S_{2n} in this approximation is shown in Fig. 1 (a) with the open circles. The total neutron density and pair densities of the box-discretized results

are shown with the dotted lines in Fig. 2 (a) and (c). The corresponding neutron r.m.s. radii $r_{\text{r.m.s.}}$ and pair r.m.s. radii $\tilde{r}_{\text{r.m.s.}}$ are shown with open circles in panels (b) and (d). The r.m.s. radii of different partial waves are also shown in Figs. 3 and 4 with open symbols for the neutron density and the pair density, respectively.

From the comparison between the continuum and the box-discretized calculations, we observe the following. The influence of the box boundary condition is seen both in the neutron density $\rho(r)$ and in the pair density $\tilde{\rho}(r)$ at $r \approx 15-20$ fm close to the box boundary (Fig. 2 (a) and (c)). However this influence causes only negligibly small difference in the bulk properties such as the total energy and its derivative, the two-neutron separation energy S_{2n} . This is because the density and the pair density of neutrons at $r \gtrsim 15$ fm are very small, and its contribution to the total energy is accordingly small. The r.m.s. radius $r_{\text{r.m.s.}}$ (Fig. 2 (b)) of the total neutron density is also affected very little by the box-discretization. If we look into the r.m.s. radii $r_{\text{r.m.s.},lj}$ for each partial waves (Fig. 3), we can see some difference in the contributions from the p -wave while the other partial waves are not affected. This indicates that the neutron density contributed from the p -wave is the most extended while other partial waves extend less (see also Fig.5). More importantly, we can see more significant difference in the neutron pair r.m.s. radii $\tilde{r}_{\text{r.m.s.}}$ and $\tilde{r}_{\text{r.m.s.},lj}$ (cf. Fig. 2 (d) and Fig. 4). The difference is seen not only in the p - and f -waves, but also in the s - and d -waves. This difference is larger for lower angular momentum states and in more neutron-rich nuclei, where we expect more continuum coupling due to the lower centrifugal barrier. It can be concluded from these observations that the proper treatment of the continuum quasiparticle states is important for the description of the tail part of the pair density, i.e. the pair correlation in the giant halo.

IV. CONTINUUM QUASIPARTICLE SPECTRA

A. Low-lying quasiparticle states

A quasiparticle state with excitation energy E in the partial wave lj has contributions to the density $\rho(r)$ and the pair density $\tilde{\rho}(r)$, which are given by [27, 28]

$$\begin{aligned}\rho_{lj}(r, E) &= \frac{(2j+1)}{4\pi r^2} \frac{1}{\pi} \text{Im} \mathcal{G}_{0,lj}^{(11)}(r, r, -E - i\epsilon), \\ \tilde{\rho}_{lj}(r, E) &= \frac{(2j+1)}{4\pi r^2} \frac{1}{\pi} \text{Im} \mathcal{G}_{0,lj}^{(12)}(r, r, -E - i\epsilon),\end{aligned}\tag{10}$$

with the use of the HFB Green's function and an infinitesimal constant ϵ . They satisfy $\rho(r) = \sum_{lj} \int dE \rho_{lj}(r, E)$ and $\tilde{\rho}(r) = \sum_{lj} \int dE \tilde{\rho}_{lj}(r, E)$. We can then define the occupation number density as a function of E by

$$n_{lj}(E) = \int 4\pi r^2 \rho_{lj}(r, E) dr, \quad (11)$$

which represents the neutron number associated with the quasiparticle state with energy E and the quantum numbers lj . We can also define the pair number density

$$\tilde{n}_{lj}(E) = \int 4\pi r^2 \tilde{\rho}_{lj}(r, E) dr, \quad (12)$$

using the pair density contribution $\tilde{\rho}_{lj}(r, E)$.

Figure 6 (a)-(d) show the occupation number density $n_{lj}(E)$ of neutron quasiparticle states in a quasiparticle energy interval $E = 0 \sim 2$ MeV for ^{126}Zr and ^{138}Zr , while Fig. 6 (e)-(h) are the neutron pair number density $\tilde{n}_{lj}(E)$ for the same isotopes. We choose $\epsilon = 10^{-10}$ MeV in Eq. (10). Note that the quasiparticle states with energy E larger than the threshold energy $|\lambda|$ form a continuum spectrum.

We can see from this figure that the quasiparticle spectra of ^{126}Zr and those of ^{138}Zr have common features. The partial waves $p_{1/2}, p_{3/2}, f_{5/2}$ and $f_{7/2}$ in panels (c), (d), (g) and (h) have peak structures with finite width, i.e., quasiparticle resonances, in the spectra of $n_{lj}(E)$ and $\tilde{n}_{lj}(E)$. These quasiparticle resonances correspond to the HF single-particle orbits which are shown in Fig.1 (b). It should be noticed here that in ^{126}Zr the HF single-particle orbits $3p_{3/2}$ and $2f_{7/2}$ are discrete bound states with very small binding energy $\varepsilon \approx -0.1 \sim -0.2$ MeV. It is the pair correlation that transforms these bound HF single-particle orbits to unbound quasiparticle resonances. Similarly, the weakly bound HF single-particle orbits $3p_{3/2}, 3p_{1/2}$ and $2f_{7/2}$ in ^{138}Zr become the quasiparticle resonances when the pair correlation is taken into account. Table 1 lists the resonance energies E_{res} of these quasiparticle resonances, which we evaluate as the peak energy of $n_{lj}(E)$.

Another noticeable feature is seen in the quasiparticle spectra of the partial waves with positive parity, $s_{1/2}, d_{3/2}, d_{5/2}$, etc, plotted in Fig. 6 (a), (b), (e) and (f). We see here smooth profiles of $n_{lj}(E)$ and $\tilde{n}_{lj}(E)$, indicating non-resonant continuum quasiparticle states. Concerning the occupation number density $n_{lj}(E)$, the positive parity non-resonant quasiparticle states have contributions which are smaller, by several orders of magnitude, than the contributions of the resonant quasiparticle states with the negative parity shown in panels (c)

and (d). On the other hand, the pair number densities $\tilde{n}_{lj}(E)$ of the positive parity partial waves ((e) and (f)) are more than ten times larger than $n_{lj}(E)$ of the same partial waves ((a) and (b)). It is also noticed that $\tilde{n}_{lj}(E)$ of the positive parity partial waves ((e) and (f)) are even comparable to those of the negative parity partial waves ((g) and (h)), except around the resonant peaks. These sizable contributions from the non-resonant $s_{1/2}$, $d_{3/2}$ and $d_{5/2}$ quasiparticles to the pair number density can be related to the non-negligible fraction $\tilde{\rho}_{lj}(r)/\tilde{\rho}(r)$ of the $s_{1/2}$, $d_{3/2}$ and $d_{5/2}$ quasiparticles in the halo tail of the pair density as shown in Fig. 5 (c) and (d).

B. Pairing gaps and missing bound quasiparticle states

In the isotopes $^{126-138}\text{Zr}$, all the quasiparticle states are embedded in the continuum energy region $E > |\lambda|$ (Fig. 6 is an example), namely there exist no bound quasiparticle states with $E < |\lambda|$ except in ^{124}Zr . [In ^{124}Zr there is only one bound quasiparticle state $3p_{3/2}$ at $E = 0.436$ MeV, which is very close to $|\lambda| = 0.446$ MeV.] It is a remarkable effect of the pair correlation since the HF single-particle states $3p_{1/2}$, $3p_{3/2}$ and $2f_{7/2}$ are all bound orbits if the pair correlation were neglected (cf. Fig. 1(b)). To understand this, we first evaluate the average pairing gaps defined as usual by $\Delta_{uv} = \int d\mathbf{r} \Delta(\mathbf{r}) \tilde{\rho}(\mathbf{r}) / \int d\mathbf{r} \tilde{\rho}(\mathbf{r})$ and $\Delta_{vv} = \int d\mathbf{r} \Delta(\mathbf{r}) \rho(\mathbf{r}) / \int d\mathbf{r} \rho(\mathbf{r})$ with two different weight factors given by the neutron density or the neutron pair density. They are listed in Table I. Their values $\Delta_{uv} \approx 0.59 - 0.68$ MeV and $\Delta_{vv} \approx 0.53 - 0.61$ MeV are fairly constant ($\Delta \approx 0.5 - 0.7$ MeV) in the interval $A = 126 - 138$, except for $\Delta \approx 0.42 - 0.47$ MeV at $A = 124$, where basically only two valence neutrons participate in the pair correlation. We observe here that the average pairing gap $\Delta \approx 0.5 - 0.7$ MeV is larger than the absolute value of the Fermi energy $|\lambda|$ in the isotopes $^{126-138}\text{Zr}$, where $|\lambda| < 0.42$ MeV. This relation $\Delta > |\lambda|$ is proposed in Ref. [4] as a criterion for a non-perturbative role of the pairing on the properties of the weakly bound nuclei. We can also examine this criterion with respect to the individual quasiparticle resonances. We here note that the energy of the quasiparticle resonances $3p_{1/2}$ and $3p_{3/2}$ satisfy $E_{\text{res}} > 0.4$ MeV and $E_{\text{res}} > |\lambda|$ in the isotopes with $A = 126 - 138$ (and similarly, $E_{\text{res}} > 0.7$ MeV and $E_{\text{res}} > |\lambda|$ for $2f_{7/2}$). As a result, if we use the BCS expression $E_{\text{res}} \approx \sqrt{(\varepsilon - \lambda)^2 + \Delta_{\text{eff}}^2}$ to relate the quasiparticle energy E_{res} and the effective pairing gap Δ_{eff} relevant to the specific quasiparticle state, we can estimate the effective pairing gap of the $3p_{1/2}$ and $3p_{3/2}$

resonances as $\Delta_{\text{eff}} \gtrsim 0.4$ MeV (and $\Delta_{\text{eff}} \gtrsim 0.7$ MeV for the $2f_{7/2}$ resonance) and $\Delta_{\text{eff}} \gtrsim |\lambda|$. [Here we used also the fact that the HF single-particle energies of $3p_{1/2}$, $3p_{3/2}$ and $2f_{7/2}$ are almost degenerate with the Fermi energy, $\varepsilon \approx \lambda$ (cf. Fig. 1).] Again we can infer the relation $\Delta_{\text{eff}} > |\lambda|$ also for the effective pairing gap of the weakly-bound orbits under consideration.

C. Width of quasiparticle resonances

We evaluate the width of a quasiparticle resonance by reading the FWHM of the peak structure in the occupation number density $n_{lj}(E)$. The resonance energies and widths of the low-lying quasiparticle resonances $3p_{1/2}$, $3p_{3/2}$, $2f_{5/2}$ and $2f_{7/2}$ are displayed in Fig. 7. The length of the bar in this plot represents the width Γ of the resonant states multiplied by a factor of 5. For the sake of reference, it also plots the threshold energy $|\lambda|$ and the position V_B of the barrier top of the HF potential including the centrifugal potential measured from the Fermi energy. We list in Table 1 the barrier height of the potential $V_{\text{max}} = V_B - |\lambda|$ and the resonance energy $e_{\text{res}} = E_{\text{res}} - |\lambda| = E_{\text{res}} + \lambda$ measured from zero HF single-particle energy.

There are at least two mechanisms that govern the width of the quasiparticle resonances. One is the barrier penetration of a single-particle motion, which is present in any potential models, i.e. the HF potential in the present case. The other is the one caused by the pair correlation, through which even bound HF single-particle orbits can couple to the scattering states. An example of the latter is known as quasiparticle resonances originating from deep hole states [4, 31].

These two mechanisms are interwoven in a rather complex way to produce the widths of the low-lying quasiparticle resonances under discussion. A typical example is seen in the isotopic dependence of the width of the $3p_{1/2}$ resonance (Fig.7 (a)). As the mass number increases from $A = 124$ to $A = 138$, the width of the $3p_{1/2}$ resonance first decreases, then turns to increase at larger neutron number $A \gtrsim 132$. The decrease of the width in the interval $124 \leq A \lesssim 132$ is hardly explained by the barrier penetration mechanism alone: the barrier height V_{max} decreases (see Table I) while the resonance energy e_{res} are fairly constant in this interval, thus the barrier penetration mechanism would lead to an "increase" of the width. The decrease of the width may be explained by combining the potential barrier penetration and the continuum coupling caused by the pairing in the following way. We here note that

because of the change in the relative ordering of the HF single-particle energy ε and the Fermi energy λ (cf. Fig.2), the particle-character of the $3p_{1/2}$ quasiparticle state, dominant at $A = 124$, is weakened gradually with increasing the mass number from $A = 124$ to $A \approx 132$, and a hole-character grows with further increase of A . If we can assume that the coupling of the hole-component $\varphi_{2,lj}(r)$ to the scattering wave via the pair potential is weaker than that of the particle-component $\varphi_{1,lj}(r)$ to the scattering wave via the barrier penetration, we then expect the decrease of the width. At the mass numbers $A \approx 132 - 134$, the barrier penetration becomes progressively effective since the resonance energy e_{res} increases, and it causes the increase of the width. However, the width remains finite even at $A = 136, 138$ where the resonance energy lies above the barrier height. In these isotopes, the width is probably controlled dominantly by the coupling to the continuum via the pair potential. These speculations remain at a qualitative level. The analytical evaluation of the width of the quasiparticle resonance is known only for those originating from deep hole states [4, 31], but our situation is more complex. Quantitative understanding of the width of the low-lying quasiparticle resonances associated with the weakly-bound single-particle orbits remains as a future subject.

D. Continuum coupling and comparison with the box discretization

It is interesting to compare the box-discretized HFB calculation and the continuum HFB calculation for the description of the resonant quasiparticle states.

The quasiparticle states are all discretized when the box boundary condition is adopted, and the discretized states corresponding to the quasiparticle resonances we are discussing are the lowest energy states in each of the partial waves $p_{1/2}, p_{3/2}, f_{5/2}$ and $f_{7/2}$. The quasiparticle energies of these states are shown in Fig.7 with open circles. We see large deviations (the deviation is even larger than the value of the resonance width) from the resonance energies E_{res} obtained in the continuum HFB calculation for the $3p_{1/2}$ and $3p_{3/2}$ states at $A \lesssim 134$. Contrastingly, at $A = 136$ and 138 , the quasiparticle energies obtained in the box-discretized calculation agree rather well with the resonance energies (the deviation is comparable with the value of the resonance width). A good agreement is also seen in the quasiparticle resonances of $2f_{7/2}$ and $2f_{5/2}$.

A hint of the large deviation is suggested in the ratio between the width Γ and the

resonance energy e_{res} . It is seen from Table I that the quasiparticle resonance $3p_{1/2}$ at $A = 124$, for instance, has a width $\Gamma = 61$ keV which is comparable to the resonance energy $e_{\text{res}} = 79$ keV, i.e., $\Gamma/e_{\text{res}} \sim 1$. This ratio decreases with A . We find that the large deviation is seen in the case of the large width-energy ratio $\Gamma/e_{\text{res}} \gtrsim 1/3$ (at $124 \leq A \lesssim 134$). The same is seen also for the $3p_{3/2}$ resonance. On the other hand, the small deviation can be linked to the small width-energy ratio $\Gamma/e_{\text{res}} \lesssim 1/5$ as seen in the $3p_{1/2}$ and $3p_{3/2}$ resonances at $A = 136$ and 138 , and also in the $2f_{5/2}$ and $2f_{7/2}$ resonances in all the isotopes. Clearly the large width-energy ratio $\Gamma/e_{\text{res}} \gtrsim 1/3$ indicates that the coupling to the continuum scattering states is strong even though the resonance energy is located below the potential barrier ($e_{\text{res}} < V_{\text{max}}$ or $E < V_B$). Consequently the bound state approximation does not work. For the same reason it is hard to describe these resonances in a box-discretized calculation unless the box size is taken sufficiently large. In order to describe the resonance at such a small energy $e_{\text{res}} \sim 50$ keV, one has to use a large box satisfying $\hbar^2/2m \times (\pi/R_{\text{box}})^2 \lesssim e_{\text{res}}$, i.e., $R_{\text{box}} \gtrsim 60$ fm. A further larger box is needed in order to describe the distribution around the peak [19] to evaluate the width, or one needs to combine with other methods, such as stabilization method [35], etc.

From the above analysis, we can conclude that the correct treatment of the continuum is important to describe the quasiparticle resonances originating from weakly bound orbits with low angular momenta.

V. EXPONENTIAL TAILS OF THE PAIR CORRELATED HALO

In this subsection, we will discuss the asymptotic behavior of the density and the pair density associated with the giant neutron halo. We have already discussed in section III that the density and the pair density exhibit extended tails which can be characterized by an exponentially decreasing behavior as a function of r . In order to understand the origins of the tail behaviors, we shall investigate the neutron density $\rho_{lj}(r)$ and the neutron pair density $\tilde{\rho}_{lj}(r)$ which are decomposed with respect to the partial waves lj .

Figure 8 (a) and (b) shows the lj -decomposed neutron density $4\pi r^2 \rho_{lj}(r)$ weighted with the volume element $4\pi r^2$ for ^{126}Zr . We already saw the dominance of the p -wave component in the halo tail region ($r \gtrsim 10$ fm) in connection with Fig. 5 in section III. Noticeably the exponential slopes in the tail region are different for different partial waves. The $p_{1/2}$ and

$p_{3/2}$ components have the most gentle slopes (hence they dominates in the tail) while the slopes of $f_{7/2}$ and $f_{5/2}$ are steeper than the p -waves. The densities arising from the s - and d -waves are much steeper, and thus their contributions to the halo tail is negligible.

Looking at the lj -decomposed neutron pair densities $4\pi r^2 \tilde{\rho}_{lj}(r)$, shown in panels (c) and (d), we immediately see that the exponential slopes of the neutron pair densities are apparently different from the slopes associated with the neutron density $\rho_{lj}(r)$ (panels (a) and (b)), and it is also obvious that the exponential slopes exhibit much weaker dependence on lj . The slopes are rather similar among the partial waves $s_{1/2}, d_{3/2}$ and $d_{5/2}$ as well as $p_{1/2}, p_{3/2}, f_{5/2}$ and $f_{7/2}$.

A. neutron density

In order to clarify the behaviors of the exponential slopes in the halo tail region, we shall quantify the exponential slope of the neutron density $\rho_{lj}(r)$. For this purpose, we consider a simple fitting function

$$r^2 \rho_{\text{fit},lj}(r) \propto \left(r h_l^{(+)}(i\kappa_{lj} r) \right)^2 \quad (13)$$

with $h_l^{(+)}(z)$ being the spherical Hankel function [37]. A concrete form for the orbital angular momentum $l = 1$ is $r^2 \rho_{\text{fit},lj}(r) = C e^{-2\kappa_{lj}r} \left[1 + \frac{1}{\kappa_{lj}r} \right]^2$. This is an asymptotic form expected to be obtained if the tail density is contributed by a single quasiparticle state with a fixed energy. (Note that the asymptotic form of the second-component wave function is $\varphi_{2,lj}(r)/r \sim h_l^{(+)}(i\kappa_{lj}r)$ with $\kappa_{lj} = \sqrt{2m(E + |\lambda|)/\hbar^2}$.) We fit this function $r^2 \rho_{\text{fit},lj}(r)$ to the numerically obtained density $r^2 \rho_{lj}(r)$ in the tail region, and we extract the parameter $2\kappa_{lj}$ that represents the exponential slope of $r^2 \rho_{lj}(r)$. A simpler choice of the fitting function would be $r^2 \rho_{\text{fit},lj}(r) = C \exp(-2\kappa_{lj}r)$ valid for $\kappa_{lj}r \gg 1$. But we do not adopt this because the effect of the centrifugal barrier is not completely negligible (i.e. $\kappa_{lj}r \gg 1$ is not realized) in the region under discussion, $r \sim 20$ fm. We use the interval $r = 15 - 20$ fm for the fit, and we denote the extracted value as $2\kappa_{lj}$, which we shall call as *asymptotic exponential constant*.

The extracted asymptotic exponential constant $2\kappa_{lj}$ is shown in Fig. 9 (a) and (b). It is noticed that the extracted values $2\kappa_{lj}$ differ for different lj , and their isotopic dependencies are also different. For instance, $2\kappa_{lj}$ for $f_{5/2}$ is obviously different from that for $f_{7/2}$ although both equally have sizable contributions to the halo density.

We shall now show that the asymptotic exponential constants $2\kappa_{lj}$ of these partial waves are governed by the low-lying quasiparticle resonances $3p_{1/2}$, $3p_{3/2}$, $2f_{5/2}$ and $2f_{7/2}$. To show this, we evaluate a part of the neutron density $\rho_{lj}(r)$, denoted by $\rho'_{lj}(r)$ below, in which we consider only contributions from the low-lying quasiparticles with $E = 0 - 3$ MeV including the resonances mentioned above. The truncated neutron density $\rho'_{lj}(r)$ can be calculated by using Eq. (7) in which the contour of the integral encloses only the quasiparticle states with $E = 0 - 3$ MeV. In Fig. 10 (a) we compare $\rho'_{lj}(r)$ with $\rho_{lj}(r)$ for $p_{3/2}$ contributions in ^{138}Zr . It is seen that $\rho'_{p_{3/2}}(r)$ reproduces $\rho_{p_{3/2}}(r)$ very nicely as far as the tail region $r > 10$ fm is concerned. We extract the asymptotic exponential constant $2\kappa'_{lj}$ for $\rho'_{p_{3/2}}(r)$ by using the same fitting function of Eq. (13), and we confirm that $2\kappa'_{lj}$ and $2\kappa_{lj}$ are almost the same. We also compare the tail of the neutron density $\rho_{lj}(r)$ with that of the density $\rho_{lj}(r, E_{\text{res}})$ which represents a contribution from the quasiparticle state at the resonance energy E_{res} (cf. Table I). It is seen in Fig. 10 that the exponential slope of $\rho_{lj}(r, E_{\text{res}})$ agrees quite well with that of $\rho_{lj}(r)$.

To be more quantitative, we compare in Fig. 9 (b) the extracted asymptotic exponential constant $2\kappa_{lj}$ of $\rho_{lj}(r)$ with the exponential constant

$$2\kappa_{lj,\text{res}} = 2\sqrt{\frac{2m(E_{\text{res}} + |\lambda|)}{\hbar^2}} \quad (14)$$

of $\rho_{lj}(r, E_{\text{res}})$, which can be calculated using the resonance energy E_{res} , for the partial waves $p_{1/2}$, $p_{3/2}$, $f_{5/2}$ and $f_{7/2}$ in all the isotopes. The agreement is very good and it is even hard to see the difference between the two in some cases. We thus confirm that the low-lying quasiparticle resonances $3p_{1/2}$, $3p_{3/2}$, $2f_{5/2}$ and $2f_{7/2}$ corresponding to the weakly-bound HF single-particle orbits dominate the tail and govern its asymptotic exponential constant.

The asymptotic exponential constants $2\kappa_{lj}$ of the $s_{1/2}$, $d_{3/2}$ and $d_{5/2}$ partial wave neutron densities behave in a different way as seen in Fig. 9 (a). Firstly, we observe the large values of $2\kappa_{lj}$, which can be attributed to the fact that the tail of $\rho_{lj}(r)$ in these partial waves is dominated by deeply bound orbits. Secondly we find that the values of $2\kappa_{lj}$ decrease steeply with increasing A . This feature can be explained by the fact that the non-resonant continuum states in the low-lying region of these partial waves contribute more as the neutron drip-line is approached. In Fig. 10 (b) we plot the truncated neutron density $\rho'_{lj}(r)$ of $s_{1/2}$ partial wave in ^{138}Zr , which represents the contributions from low-lying non-resonant continuum states. Although $\rho'_{lj}(r)$ is smaller than $\rho_{lj}(r)$ by several orders, it dominates the far external part

($r \gtrsim 15$ fm) of the total density $\rho_{lj}(r)$. Note, however, that the $s_{1/2}$, $d_{3/2}$ and $d_{5/2}$ densities do not influence the tail of the total neutron density as their relative contributions are negligible in comparison with those contributed from the low-lying p , f -wave quasiparticle resonances. Therefore, the complex behavior of $2\kappa_{lj}$ in the s , d -wave does not affect the conclusion on the dominance of the low-lying quasiparticle resonances in the exponential tail of the neutron densities.

B. neutron pair density

Let us now examine the asymptotic exponential constants of the neutron pair densities $\tilde{\rho}_{lj}(r)$. Similarly to the neutron density $\rho_{lj}(r)$, we fit an exponentially decreasing function to the numerically obtained neutron pair density $\tilde{\rho}_{lj}(r)$, but we need a proper fitting function other than $\rho_{\text{fit},lj}(r)$ (Eq.(13)) which is appropriate only for the normal density. We adopt

$$r^2 \tilde{\rho}_{\text{fit},lj}(r) \propto r h_l^{(+)}(i\tilde{\kappa}_{lj}r) \quad (15)$$

as a fitting function. Specifically, for $l = 1$, we have $r^2 \tilde{\rho}_{\text{fit},lj}(r) = \tilde{C} e^{-\tilde{\kappa}_{lj}r} \left[1 + \frac{1}{\tilde{\kappa}_{lj}r}\right]$. This functional form is based on the following considerations. We first point out that there is no simple estimate for the asymptotic form of the pair density. Even if we assume that a quasiparticle state with energy E contributes to the pair density, the contribution $r^2 \tilde{\rho}_{lj}(r, E) \propto \varphi_{1,lj}(r) \varphi_{2,lj}(r)$ does not have an exponential form since the first-component wave function $\varphi_{1,lj}(r)$ is an oscillating sinusoidal function in the asymptotic region as the quasiparticle states under consideration are all embedded above the threshold energy. We therefore exploit only the asymptotic form of $\varphi_{2,lj}(r)$, which behaves as $\varphi_{2,lj}(r) \sim r h_l^{(+)}(i\tilde{\kappa}_{lj}r)$, to prepare the fitting function. We use the same interval $r = 15 - 20$ fm for the fitting, and denote the extracted asymptotic exponential constant as $\tilde{\kappa}_{lj}$ for the pair density.

The extracted value of the asymptotic exponential constant $\tilde{\kappa}_{lj}$ is plotted in Fig. 9 (c) and (d). It is seen here that the behaviors of $\tilde{\kappa}_{lj}$ are different from those of the asymptotic exponential constants $2\kappa_{lj}$ of the neutron densities $\rho_{lj}(r)$. This immediately demonstrates that the quasiparticle resonances are not the major origin of the exponential tail of the pair densities $\tilde{\rho}_{lj}(r)$. It is also seen that the values of $\tilde{\kappa}_{lj}$ for all the partial waves $s_{1/2}$, $p_{1/2}$, $p_{3/2}$, $d_{3/2}$, $d_{5/2}$, $f_{5/2}$ and $f_{7/2}$ are rather similar, and they all exhibit similar isotopic

dependencies.

It is useful here to refer to the argument in Ref. [4] which asserts that the asymptotic exponential constant of the pair density may be given by

$$\tilde{\kappa}_{\min} = \sqrt{\frac{4m|\lambda|}{\hbar^2}} . \quad (16)$$

This is based on the consideration that the asymptotic behavior of the pair density is governed by the contribution of the lowest energy quasiparticle state, and in the case of nuclei near the drip-line, the lowest energy quasiparticle state is the continuum state with $E = |\lambda|$ (cf. Eq. (14)). In fact we see in Fig. 9 (c) and (d) that the isotopic dependencies of $\tilde{\kappa}_{lj}$ has some resemblance to that of $\tilde{\kappa}_{\min}$ although a difference by a factor of about 2 is seen here. We thus deduce that non-resonant continuum quasiparticle states dominates the asymptotic tail of the pair density, although the difference by a factor of ~ 2 suggests something beyond the argument in Ref. [4].

Figure 10 (c) and (d) are made to check the above deduction. In these panels we compare the neutron pair density $\tilde{\rho}_{lj}(r)$ with the truncated pair density $\tilde{\rho}'_{lj}(r)$ where only the low-lying quasiparticle states with $E < 3$ MeV are included in the sum of Eq. (7). It is also compared in panel (c) with the pair density $\tilde{\rho}_{lj}(r, E_{\text{res}})$ that originates from the single quasiparticle state at the resonance energy E_{res} for $p_{3/2}$ partial wave. It is seen that $\tilde{\rho}_{lj}(r, E_{\text{res}})$ apparently fails to describe the exponential tail since $\varphi_{1,lj}(r, E_{\text{res}})$ and hence $\tilde{\rho}_{lj}(r, E_{\text{res}})$ oscillate with r . On the other hand the exponential tail of the pair density $\tilde{\rho}_{lj}(r)$ is nicely reproduced by the pair density $\tilde{\rho}'_{lj}(r)$ truncated with $E < 3$ MeV. This observation applies to the pair densities of all the p, f and s, d waves (see Fig. 10 (d) for $s_{1/2}$). Recall that the s, d -waves have only non-resonant quasiparticle states in the low-lying spectrum $E < 3$ MeV. We thus conclude that the non-resonant continuum quasiparticle states dominate the asymptotic exponential tail of the neutron pair density. It is in contrast to that of the neutron density in which the low-lying quasiparticle resonances dominate. It is also concluded that the exponential tail of the pair density is governed by coherent superpositions of the contributions from the non-resonant continuum quasiparticle states near the threshold energy. Under this situation, we can evaluate approximately the exponential tail arising from the non-resonant continuum quasiparticle states as

$$r^2 \tilde{\rho}_{lj}(r) = \int_{|\lambda|} dE \varphi_{1,lj}(r, E) \varphi_{2,lj}(r, E) \sim \int_0 de \sin(kr) e^{-\kappa r} \quad (17)$$

with $k = \sqrt{2me/\hbar^2}$, $\kappa = \sqrt{2m(2|\lambda| + e)/\hbar^2}$ and $e = E - |\lambda|$. Since the weight factor $e^{-\kappa r}$ is dominant in an interval $0 < e \lesssim |\lambda|$, the superposition of non-resonant continuum wave $\sin(kr)$ with such a weight factor gives $\sim e^{-\tilde{\kappa}_{\text{nr}} r}$ with $\tilde{\kappa}_{\text{nr}} \sim O(\tilde{\kappa}_{\text{min}})$. Consequently we can expect $\tilde{\rho}_{lj}(r) \sim e^{-\tilde{\kappa}_{lj} r}$ with $\tilde{\kappa}_{lj} = \tilde{\kappa}_{\text{min}} + \tilde{\kappa}_{\text{nr}} \sim 2\tilde{\kappa}_{\text{min}}$. This estimation is in qualitative agreement with the observation $\tilde{\kappa}_{lj} \approx 2\tilde{\kappa}_{\text{min}}$ seen in the extracted asymptotic exponential constant $\tilde{\kappa}_{lj}$ (cf. Fig. 9 (c) and (d)).

VI. CONCLUSIONS

We have investigated the pair correlation in $^{124-138}\text{Zr}$ by using the self-consistent continuum Skyrme Hartree-Fock-Bogoliubov (HFB) approach, in which the asymptotic behaviors of the wave functions of the continuum quasiparticle states are properly treated with the Green's function method. The giant neutron halos in these very neutron-rich weakly-bound nuclei are analyzed in detail. Focuses are put on properties of the halo part of the neutron pair condensate, i.e. the exponential tail of the neutron pair density $\tilde{\rho}(r)$, in particular, the r.m.s. radius, its single-particle composition, and the exponential slope parameter (the asymptotic exponential constant). We found that these are apparently different from the corresponding quantities associated with the exponential tail of the neutron density $\rho(r)$.

In order to clarify the origin of the differences, we have looked into the spectrum of the neutron quasiparticle states. Because of the small Fermi energy λ and of the relative largeness of the pairing gap $\Delta \gtrsim |\lambda|$, all the quasiparticle states in $^{126-138}\text{Zr}$ are located above the threshold energy. Typical examples are the quasiparticle resonances $3p_{1/2}, 3p_{3/2}$ and $2f_{7/2}$, which play central roles in forming the giant neutron halo. They originate from the weakly bound orbits in the Hartree-Fock (HF) potential, but they appear as resonances with finite width once the pair correlation is taken into account. There exist non-resonant continuum quasiparticle states, and they contribute also to the giant halo. Such quasiparticle states are seen in all the partial waves, and typically in $s_{1/2}, d_{3/2}$ and $d_{5/2}$.

The central finding in the present analysis is that the exponential tail of the neutron pair density $\tilde{\rho}_{lj}(r)$ is contributed mainly from the low-lying non-resonant continuum quasiparticle states. This is contrasting to the microscopic structure of the exponential tail of the neutron density $\rho_{lj}(r)$, the main contributions of which are from the low-lying quasiparticle resonances $3p_{1/2}, 3p_{3/2}$ and $2f_{7/2}$ as well as $2f_{5/2}$, all corresponding to the HF orbits and

resonances near the Fermi energy.

The different microscopic origins of the neutron density $\rho_{lj}(r)$ and of the neutron pair density $\tilde{\rho}_{lj}(r)$ reflect to the asymptotic exponential constants $2\kappa_{lj}$ and $\tilde{\kappa}_{lj}$ parameterizing the exponential slope of the tail of the neutron density $\rho_{lj}(r)$ and the neutron pair density $\tilde{\rho}_{lj}(r)$, respectively. Concerning the neutron density $\rho_{lj}(r)$ of the dominant partial waves $p_{1/2}$ and $p_{3/2}$, subdominant $f_{5/2}$ and $f_{7/2}$, we found that the constant $2\kappa_{lj}$ is governed essentially by the peak energy of the lowest-lying quasiparticle resonance that arises from the bound or resonant HF single-particle orbit closest to the Fermi energy. The asymptotic exponential constant $\tilde{\kappa}_{lj}$ of the neutron pair density $\tilde{\rho}_{lj}(r)$ has a close relation to the threshold energy $|\lambda|$ of the non-resonant continuum states, rather than the energies of the low-lying quasiparticle resonances, since the superpositions of the non-resonant continuum quasiparticle states dominate the tail of $\tilde{\rho}_{lj}(r)$.

In the present analysis, we have also put a focus on the comparison between the continuum HFB calculation with the box-discretized HFB calculation. This comparison has pointed to a few specific problems of the box calculation, which arise if the size of the box is not sufficiently large. One is that the finite box causes relatively large error in describing the exponential halo tail of the neutron pair density $\tilde{\rho}_{lj}(r)$, in comparison with the tail of the neutron density $\rho_{lj}(r)$. This is because the halo tail of the neutron pair density $\tilde{\rho}_{lj}(r)$, which is dominated by the contributions of the non-resonant continuum quasiparticle states with small asymptotic kinetic energies $e = E - |\lambda|$, is more extended than the neutron density $\rho_{lj}(r)$. Another problem is found in describing the quasiparticle resonances corresponding to the weakly-bound $3p_{1/2}$ and $3p_{3/2}$ orbits, in particular in the isotopes with $A \lesssim 132$. We here have only small centrifugal barriers in the p -waves, which makes the coupling to the scattering states strong. Consequently, the quasiparticle resonances $3p_{1/2}$ and $3p_{3/2}$ are not represented well by any eigen states in the discretized calculation with a small box.

Acknowledgments

This work was partly supported by the Major State 973 Program 2013CB834400; the National Natural Science Foundation of China under Grants No. 10975007, No. 10975008, No. 11005069, and No. 11175002; the Research Fund for the Doctoral Program of Higher Education under Grant No. 20110001110087; the Oversea Distinguished Professor Project from

Ministry of Education No. MS2010BJDX001, and the Grant-in-Aid for Scientific Research (Nos. 21340073 and 23540294) from the Japan Society for the Promotion of Science.

- [1] I. Tanihata, *et al.*, Phys. Rev. Lett. **55**, 2676 (1985).
- [2] J. Meng and P. Ring, Phys. Rev. Lett. **80**, 460 (1998).
- [3] J. Dobaczewski, H. Flocard and J. Treiner, Nucl. Phys. A **422**, 103 (1984).
- [4] J. Dobaczewski, W. Nazarewicz, T. R. Werner, J. F. Berger, C. R. Chinn, and J. Dechargé, Phys. Rev. C **53**, 2809 (1996).
- [5] M. Bender, P.-H. Heenen, and P.-G. Reinhard, Rev. Mod. Phys. **75**, 121 (2003).
- [6] A. Bulgac, preprint FT-194-1980, Bucharest, 1980, nucl-th/9907088.
- [7] J. Meng and P. Ring, Phys. Rev. Lett. **77**, 3963 (1996).
- [8] D. Vretenar, A. V. Afanasjev, G. A. Lalazissis, and P. Ring, Phys. Rep. **409**, 101 (2005).
- [9] J. Meng, H. Toki, S.-G. Zhou, S. Q. Zhang, W. H. Long, and L. S. Geng, Prog. Part. Nucl. Phys. **57**, 470 (2006).
- [10] J. Meng, Nucl. Phys. A **635**, 3 (1998).
- [11] S. Q. Zhang, J. Meng, and S.-G. Zhou, Sci. China Ser. G **46**, 632 (2003).
- [12] J. Meng, H. Toki, J. Y. Zeng, S. Q. Zhang, and S.-G. Zhou, Phys. Rev. C **65**, 041302(R) (2002).
- [13] J. Terasaki, S. Q. Zhang, S.-G. Zhou, and J. Meng, Phys. Rev. C **74**, 054318 (2006).
- [14] S.-G. Zhou, J. Meng, and P. Ring, Phys. Rev. C **68**, 034323 (2003).
- [15] S.-G. Zhou, J. Meng, P. Ring, and E.-G. Zhao, Phys. Rev. C **82**, 011301(R) (2010).
- [16] W. H. Long, P. Ring, N. Van Giai, and J. Meng, Phys. Rev. C **81**, 024308 (2010).
- [17] L. L. Li, J. Meng, P. Ring, E.-G. Zhao, and S.-G. Zhou, Phys. Rev. C **85**, 024312 (2012).
- [18] Y. Chen, L. L. Li, H. Z. Liang, and J. Meng, Phys. Rev. C **85**, 067301 (2012).
- [19] K. Bennaceur, J. Dobaczewski, and M. Ploszajczak, Phys. Lett. B **496**, 154 (2000).
- [20] J. Dobaczewski, W. Nazarewicz, and P.-G. Reinhard, Nucl. Phys. A **693**, 361 (2001).
- [21] M. Grasso, N. Sandulescu, N. Van Giai and R. J. Liotta, Phys. Rev. C **64**, 064321 (2001).
- [22] I. Hamamoto and B. R. Mottelson, Phys. Rev. C **68**, 034312 (2003).
- [23] I. Hamamoto and B. R. Mottelson, Phys. Rev. C **69**, 064302 (2004).
- [24] M. Matsuo, K. Mizuyama, and Y. Serizawa, Phys. Rev. C **71**, 064326 (2005).

- [25] M. Yamagami, Phys. Rev. C **72**, 064308 (2005).
- [26] M. Grasso, S. Yoshida, N. Sandulescu, and N. Van Giai, Phys. Rev. C **74**, 064317 (2006).
- [27] H. Oba and M. Matsuo, Phys. Rev. C **80**, 024301 (2009).
- [28] Y. Zhang, M. Matsuo, and J. Meng, Phys. Rev. C **83**, 054301 (2011).
- [29] K. Hagino and H. Sagawa, Phys. Rev. C **84**, 011303(R) (2011).
- [30] W. H. Long, P. Ring, J. Meng, N. Van Giai, and C. A. Bertulani, Phys. Rev. C **81**, 031302(R) (2010).
- [31] S. T. Belyaev, A. V. Smirnov, S. V. Tolokonnikov and S. A. Fayans, Sov. J. Nucl. Phys. **45**, 783 (1987).
- [32] S. C. Yang, J. Meng and S.-G. Zhou, Chinese Phys. Lett **18**,196 (2001).
- [33] S. S. Zhang, J. Meng, S.-G. Zhou, and G. C. Hillhouse, Phys. Rev. C **70**, 034308 (2004).
- [34] L. Zhang, S.-G. Zhou, J. Meng, and E. G. Zhao, Phys. Rev. C **77**, 014312 (2008).
- [35] J. C. Pei, A. T. Kruppa, and W. Nazarewicz, Phys. Rev. C **84**, 024311 (2011).
- [36] N. Michel, K. Matsuyanagi, and M. Stoitsov, Phys. Rev. C **78**, 044319 (2008).
- [37] A. Messiah, *Quantum Mechanics*, North Holland, Amsterdam, 1962.
- [38] E. Chabanat, P. Bonche, P. Haensel, J. Meyer, and R. Schaeffer, Nucl. Phys. A **635**, 231 (1998).
- [39] J. Meng, Phys. Rev. C **57**, 1229 (1998).
- [40] M. Matsuo, Phys. Rev. C **73**, 044309 (2006).
- [41] M. Matsuo, Y. Serizawa, and K. Mizuyama, Nucl. Phys. A **788**, 307c (2007).
- [42] M. Matsuo and Y. Serizawa, Phys. Rev. C **82**, 024318 (2010).
- [43] H. Shimoyama and M. Matsuo, Phys. Rev. C **84**, 044317 (2011).

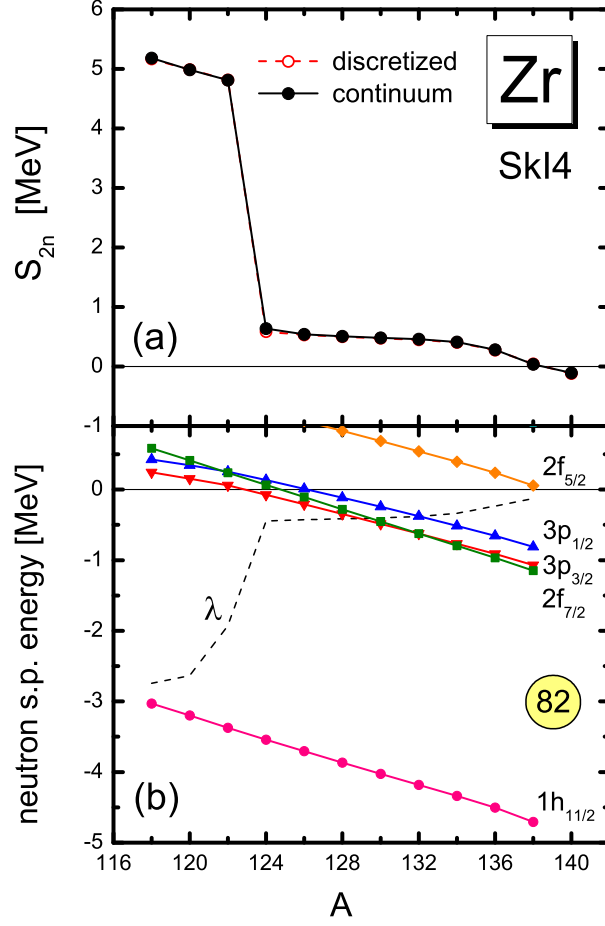


FIG. 1: (a) Two neutron separation energy S_{2n} obtained in the continuum (filled circle) and box-discretized (open circle) Skyrme Hartree-Fock-Bogoliubov (HFB) calculations for neutron-rich Zr isotopes with $A = 118 - 138$. (b) Neutron Hartree-Fock (HF) single-particle energy ε of Zr isotopes around the Fermi energy, which is given by the eigen solution of HF Hamiltonian h after the final convergence of the continuum HFB calculation. The dashed line denotes the Fermi energy λ .

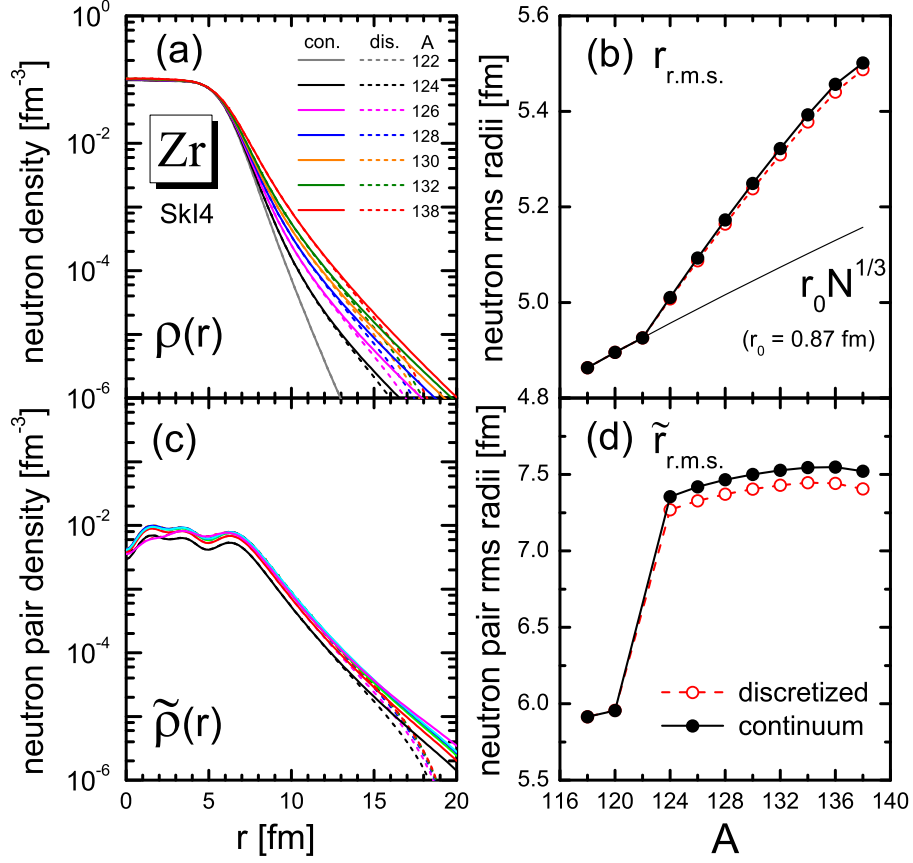


FIG. 2: (a) Neutron density $\rho(r)$, (b) neutron root-mean-square (r.m.s.) radius $r_{\text{r.m.s.}}$, (c) neutron pair density $\tilde{\rho}(r)$ and (d) neutron pair r.m.s. radius $\tilde{r}_{\text{r.m.s.}}$ for Zr isotopes. The solid lines and the filled circles are the results of the continuum HFB calculation while the dotted lines and the open circles are those obtained in the box-discretized HFB calculation.

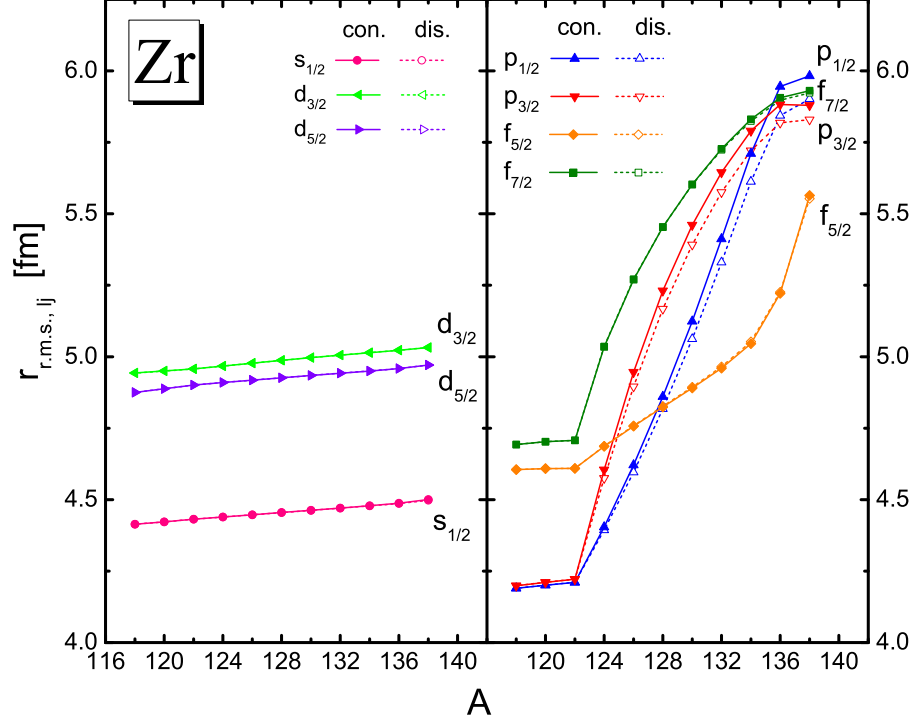


FIG. 3: Neutron root-mean-square radius $r_{r.m.s.,lj}$ of the s , p , d and f partial waves of Zr isotopes calculated for the lj -decomposed neutron density $\rho_{lj}(r)$. The filled symbols are the results obtained in the continuum HFB calculation while the open symbols are the results obtained in the box-discretized HFB calculation.

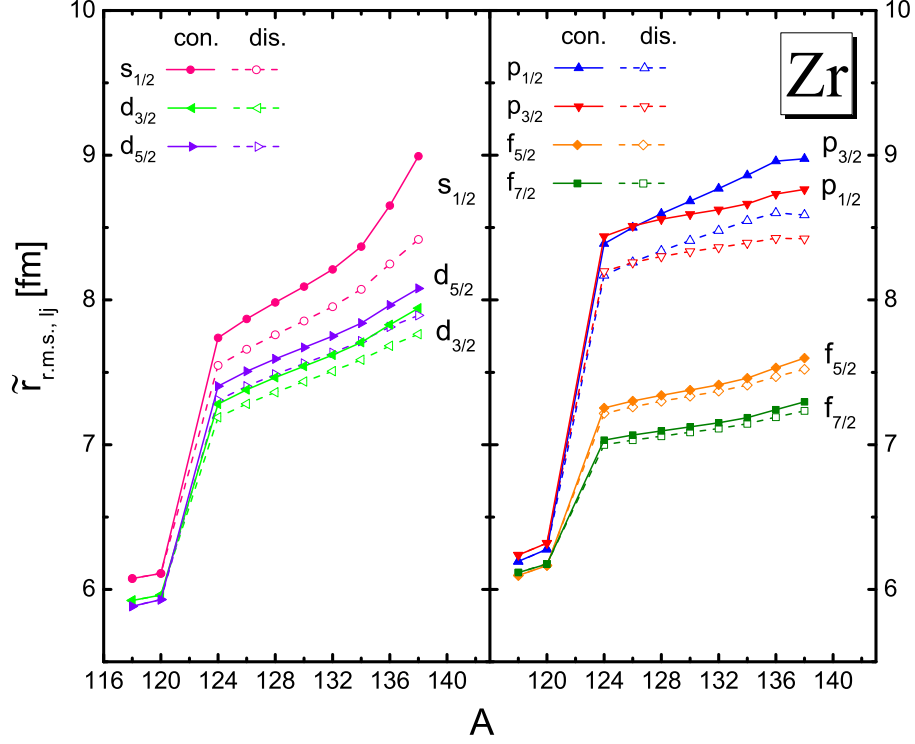


FIG. 4: Neutron pair root-mean-square radius $\tilde{r}_{\text{r.m.s.},lj}$ of the s , p , d and f partial waves of Zr isotopes calculated for the lj -decomposed neutron pair density $\tilde{\rho}_{lj}(r)$. The filled symbols are the results obtained in the continuum HFB calculation while the open symbols are the results obtained in the box-discretized HFB calculation.

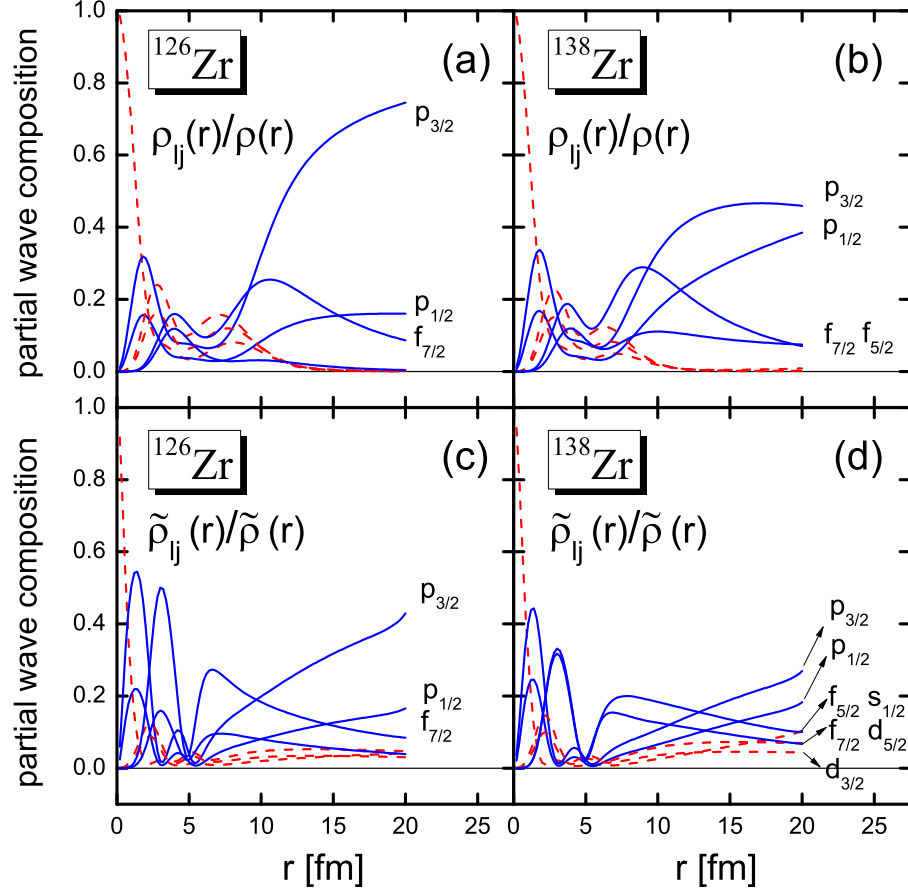


FIG. 5: Compositions of different partial waves to the total neutron density, $\rho_{lj}(r)/\rho(r)$, as a function of the radial coordinate r for ^{126}Zr (panel (a)) and ^{138}Zr (panel (b)). The solid lines denote the negative parity states, and the dashed lines the positive parity states. The same plot for the neutron pair density, $\tilde{\rho}_{lj}(r)/\tilde{\rho}(r)$, for ^{126}Zr (panel (c)) and ^{138}Zr (panel (d)).

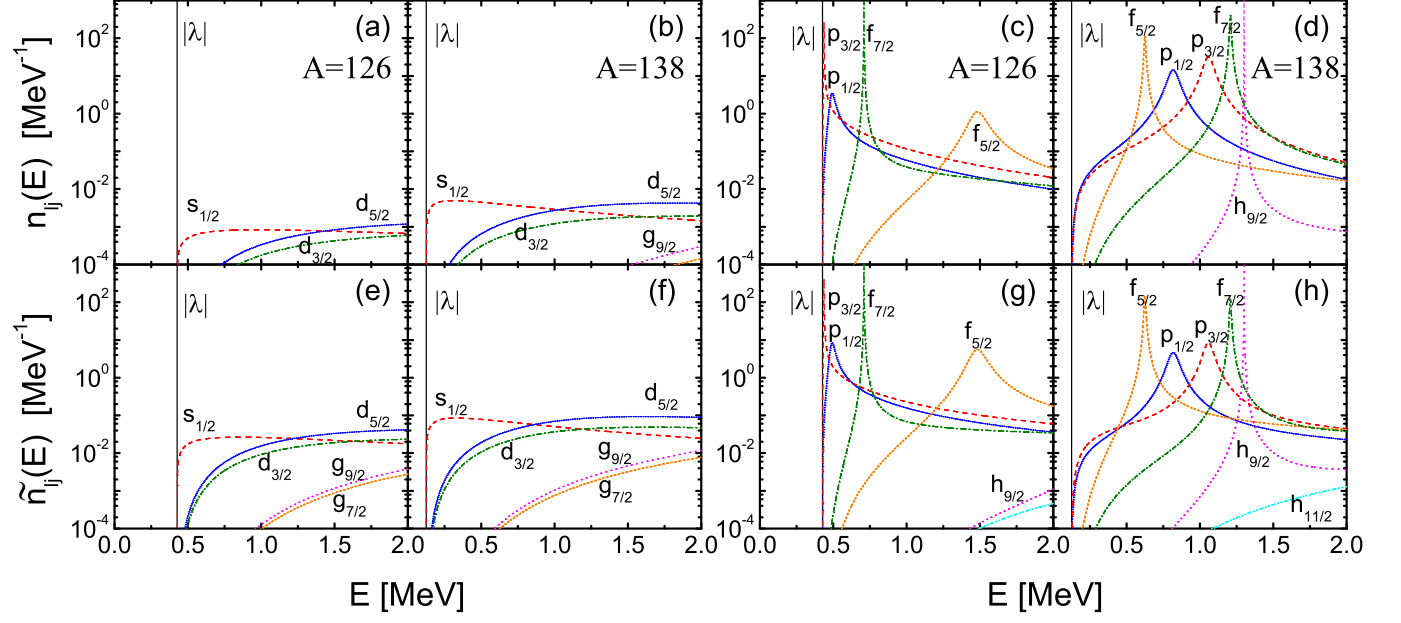


FIG. 6: Occupation number densities $n_{lj}(E)$ (panels (a) and (c)) and pair number densities $\tilde{n}_{lj}(E)$ (panels (e) and (g)) of neutron quasiparticle states for different partial waves of ^{126}Zr , while panels (b), (d), (f), and (h) are the same quantities but for ^{138}Zr . The vertical line indicates the threshold energy $|\lambda|$ for the continuum quasiparticle states.

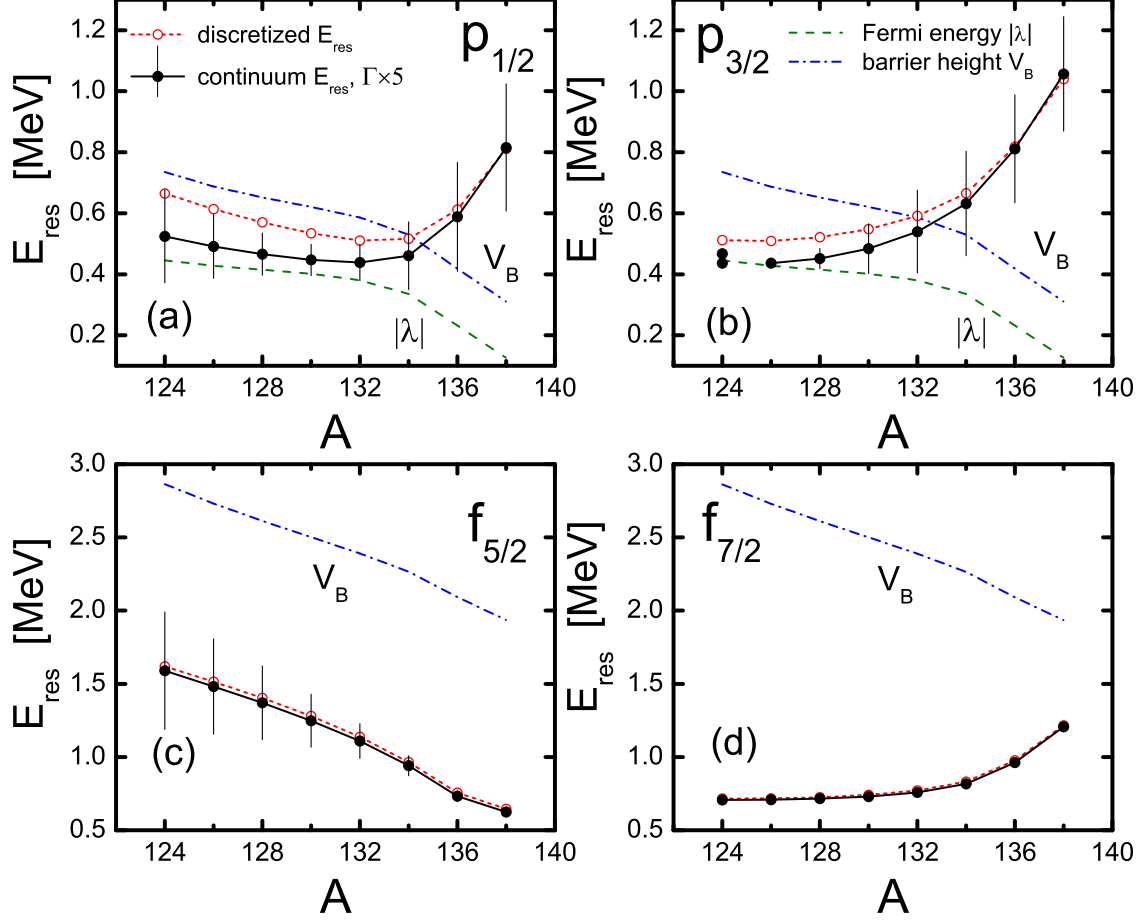


FIG. 7: Peak energy E_{res} and the width Γ of the resonant quasiparticle states around the Fermi energy in the $p_{1/2}$, $p_{3/2}$, $f_{5/2}$, and $f_{7/2}$ partial waves, plotted in panels (a), (b), (c) and (d) respectively, obtained for the Zr isotopes with $A = 124 - 138$. The filled circles are the resonance energy E_{res} , and the vertical bars represent the width Γ multiplied by a factor of 5. The open circles are discretized quasiparticle energies obtained in the box-discretized HFB calculation. The dashed line in panels (a) and (b) is the threshold $|\lambda|$ for the continuum quasiparticle states. The dash-dotted line in each panel denotes the position V_B of the barrier top of the HF potential including the centrifugal potential measured from the Fermi energy.

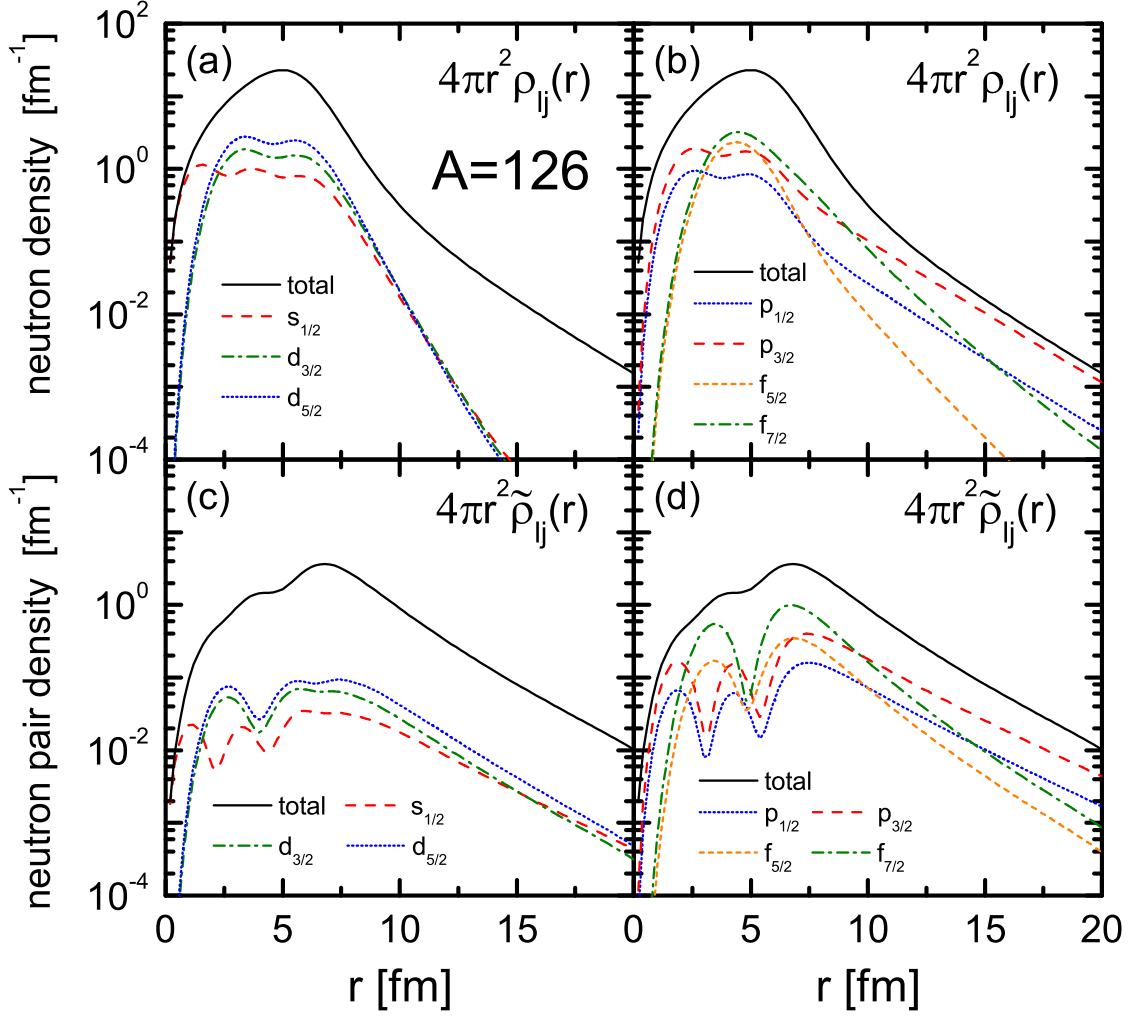


FIG. 8: (a)-(b) Neutron density $4\pi r^2 \rho_{lj}(r)$ and (c)-(d) neutron pair density $4\pi r^2 \tilde{\rho}_{lj}(r)$ of the $s_{1/2}$, $p_{1/2}$, $p_{3/2}$, $d_{3/2}$, $d_{5/2}$, $f_{5/2}$, and $f_{7/2}$ partial waves in ^{126}Zr . The total neutron density $4\pi r^2 \rho(r)$ and neutron pair density $4\pi r^2 \tilde{\rho}(r)$ are also plotted with the solid line.

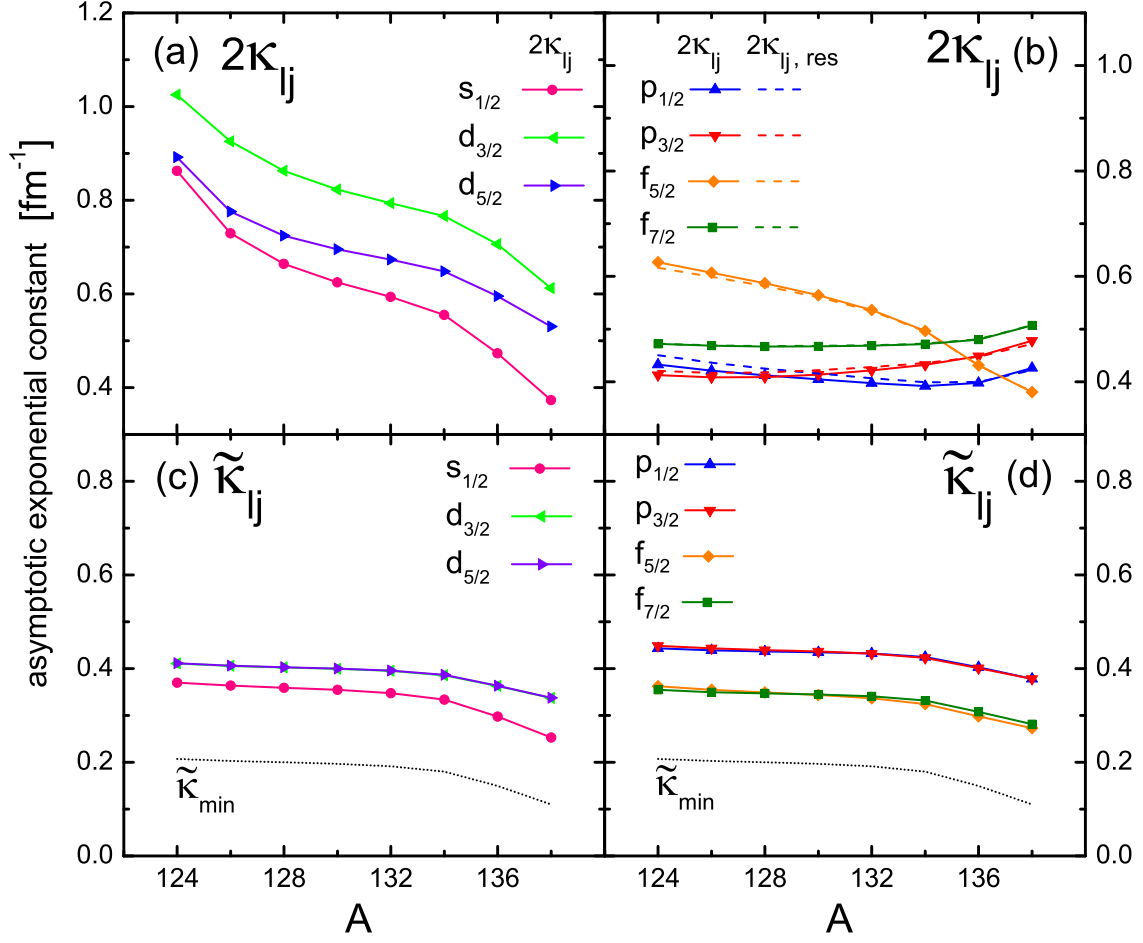


FIG. 9: (a) (b) Asymptotic exponential constant $2\kappa_{lj}$ of the neutron density $\rho_{lj}(r)$, and (c) (d) $\tilde{\kappa}_{lj}$ of the neutron pair density $\tilde{\rho}_{lj}(r)$ for the $s_{1/2}$, $p_{1/2}$, $p_{3/2}$, $d_{3/2}$, $d_{5/2}$, $f_{5/2}$, and $f_{7/2}$ partial waves in the Zr isotopes. The fitting interval is $r = 15 \sim 20$ fm. The estimated asymptotic exponential constant $2\kappa_{lj, \text{res}}$ and $\tilde{\kappa}_{\text{min}}$ are also shown with the dashed line and dotted line, respectively, where $\tilde{\kappa}_{\text{min}} = \sqrt{4m|\lambda|}/\hbar$ and $\kappa_{lj, \text{res}} = \sqrt{2m(E_{\text{res}} + |\lambda|)/\hbar^2}$ are evaluated using the Fermi energy λ and the resonance energy E_{res} shown in Table I.

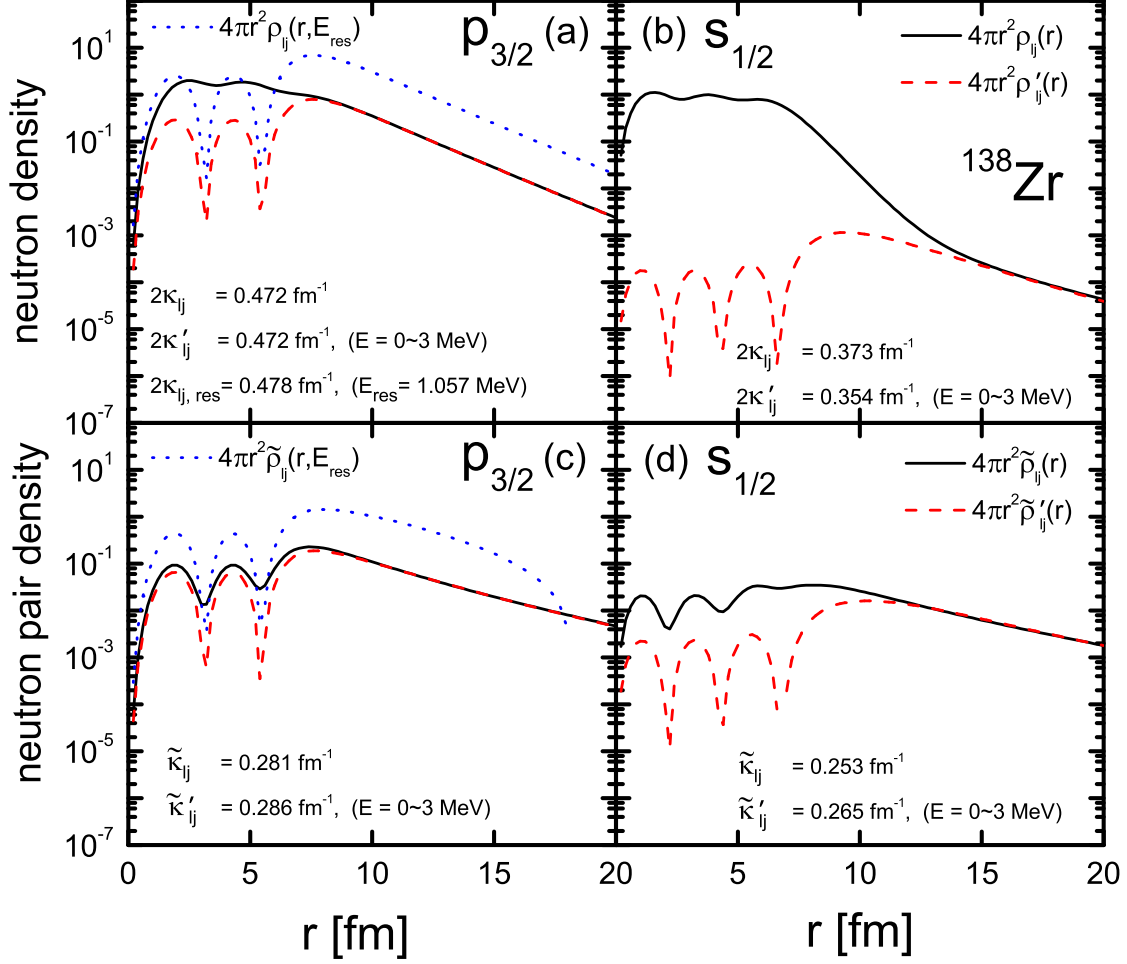


FIG. 10: (a) (b) Neutron density $4\pi r^2 \rho_{l_j}(r)$ (solid line), and the truncated neutron density $4\pi r^2 \rho'_{l_j}(r)$ contributed from the low lying quasiparticle states with $E < 3$ MeV (dashed line) (a) for $p_{3/2}$ partial wave and (b) for $s_{1/2}$ partial wave in ^{138}Zr . The contribution $4\pi r^2 \rho_{l_j}(r, E_{\text{res}})$ of the quasiparticle state at the resonance energy $E_{\text{res}} = 1.057$ MeV is also shown (dotted line) for $p_{3/2}$ in panel (a). The asymptotic exponential constant $2\kappa_{l_j}$ fitted to the neutron density $4\pi r^2 \rho_{l_j}(r)$, $2\kappa'_{l_j}$ fitted to $4\pi r^2 \rho'_{l_j}(r)$, and $2\kappa_{l_j, \text{res}}$ calculated with Eq. (14) for $p_{3/2}$ partial wave are labeled in the corresponding panels. (c) (d) The same as (a) (b) but for the neutron pair densities $4\pi r^2 \tilde{\rho}_{l_j}(r)$, $4\pi r^2 \tilde{\rho}'_{l_j}(r)$ and $4\pi r^2 \tilde{\rho}_{l_j}(r, E_{\text{res}})$. Note that the unit of the vertical axis is $[\text{fm}^{-1}]$ for $4\pi r^2 \rho_{l_j}(r)$, $4\pi r^2 \rho'_{l_j}(r)$, $4\pi r^2 \tilde{\rho}_{l_j}(r)$ and $4\pi r^2 \tilde{\rho}'_{l_j}(r)$, but $[\text{fm}^{-1} \text{ MeV}^{-1}]$ for $4\pi r^2 \rho_{l_j}(r, E_{\text{res}})$ and $4\pi r^2 \tilde{\rho}_{l_j}(r, E_{\text{res}})$.

TABLE I: Fermi energy λ and the average pairing gaps Δ_{uv} and Δ_{vv} for the Zr isotopes. Listed are also barrier height of the Hartree-Fock (HF) plus centrifugal potential V_{\max} , HF single-particle energies ε , resonance energies E_{res} and $e_{\text{res}} = E_{\text{res}} - |\lambda| = E_{\text{res}} + \lambda$, and width Γ of quasiparticle resonances around the Fermi energy for each isotope. All in MeV.

A	124	126	128	130	132	134	136	138
λ	-0.446	-0.427	-0.415	-0.401	-0.380	-0.336	-0.232	-0.126
Δ_{uv}	0.468	0.596	0.656	0.678	0.667	0.628	0.585	0.619
Δ_{vv}	0.416	0.532	0.589	0.611	0.605	0.574	0.539	0.577
$3p_{1/2} V_{\max}$	0.289	0.260	0.237	0.220	0.206	0.195	0.187	0.184
ε	0.134	0.012	-0.114	-0.244	-0.377	-0.513	-0.656	-0.810
E_{res}	0.524	0.491	0.466	0.447	0.438	0.461	0.589	0.815
e_{res}	0.079	0.064	0.051	0.045	0.058	0.125	0.357	0.690
Γ	0.061	0.042	0.028	0.021	0.024	0.044	0.072	0.083
$3p_{3/2} V_{\max}$	0.289	0.260	0.237	0.220	0.206	0.195	0.187	0.184
ε	-0.074	-0.209	-0.346	-0.485	-0.625	-0.766	-0.911	-1.069
E_{res}	0.436	0.437	0.452	0.484	0.540	0.632	0.811	1.057
e_{res}	-0.010	0.009	0.037	0.083	0.159	0.296	0.579	0.931
Γ	—	0.002	0.013	0.033	0.054	0.068	0.071	0.075
$2f_{5/2} V_{\max}$	2.418	2.304	2.198	2.100	2.011	1.931	1.860	1.810
ε	1.112	0.973	0.831	0.687	0.541	0.393	0.238	0.058
E_{res}	1.590	1.482	1.370	1.248	1.109	0.941	0.732	0.624
e_{res}	1.144	1.054	0.955	0.846	0.729	0.605	0.500	0.498
Γ	0.160	0.130	0.100	0.072	0.047	0.027	0.015	0.012
$2f_{7/2} V_{\max}$	2.416	2.302	2.197	2.099	2.009	1.930	1.859	1.809
ε	0.066	-0.106	-0.279	-0.452	-0.624	-0.796	-0.968	-1.148
E_{res}	0.708	0.709	0.715	0.730	0.758	0.816	0.963	1.207
e_{res}	0.262	0.282	0.301	0.328	0.378	0.480	0.731	1.081
Γ	0.001	0.001	0.002	0.002	0.002	0.003	0.006	0.012